Photoemission and STM study of the electronic structure of Nb-doped TiO$_2$

D. Morris, Y. Dou, J. Rebane, C. E. J. Mitchell, and R. G. Egdell[*]

Inorganic Chemistry Laboratory, South Parks Road, Oxford OX1 3QR, United Kingdom

D. S. L. Law

Research Unit for Surfaces, Transforms and Interfaces, Daresbury Laboratory, Warrington, Cheshire WA4 4AD, United Kingdom

A. Vittadini

CSSRCC-CNR, via Marzolo 1, I-35131 Padova, Italy

M. Casarin

Dipartimento di Chimica Inorganica, Metallorganica ed Analitica, Via Loredan 4, I-35131 Padova, Italy

(Received 3 November 1999)

High-resolution core- and valence-level photoemission spectra of Nb-doped TiO$_2$ ceramics (Ti$_{1-x}$Nb$_x$O$_2$ with $0.01 < x < 0.8$) have been measured using monochromatic x-ray excitation. Nb doping produces a well-defined photoemission peak in the bulk band gap of rutile, whose intensity increases with increasing doping level. Core-level spectroscopy shows that the Nb is incorporated within the rutile lattice at low doping levels mainly as Nb(V) and that the gap state is associated with Ti(III) ions. This conclusion is reinforced by variable energy photoemission measurements on Ti$_{0.9}$Nb$_{0.1}$O$_2$ in the vicinity of the Ti $3p$ and Nb $4p$ core thresholds. The photoemission resonance profile for the gap states reaches half maximum intensity at the same energy as found for oxygen-deficient TiO$_{2-x}$ but is shifted from the resonance profile for the Nb $4d$ states of NbO$_2$. STM images on Nb-doped TiO$_2$(110) are considered in relation to the spectroscopic measurements. Nb dopant atoms are imaged as ''bright spot'' clusters, implying delocalization of charge from Nb onto neighboring Ti ions. The experimental x-ray photoelectron spectroscopy data are compared with density-of-states profiles derived from local-density approximation calculations on pure and Nb-doped TiO$_2$ clusters. These calculations show that Nb doping of TiO$_2$ introduces new states of mixed Nb $4d$–Ti $3d$ character above the O $2p$ valence band of the host material. In addition, there is increased x-ray photoemission intensity across the O $2p$ valence band owing to strong Nb $4d$/O $2p$ hybridization and a cross section for ionization of Nb $4d$ states that is an order of magnitude larger than that for O $2p$ or Ti $3d$ states.

I. INTRODUCTION

Stoichiometric rutile (TiO$_2$) is an insulator with a band gap of 3.06 eV at room temperature. The titanium ion achieves it maximal oxidation state and in a formal sense, rutile can be classified as a $3d^0$ oxide. The electronic properties of d^0 materials are strongly influenced by the introduction of new donor states into the band gap of the host material either by substitutional replacement of the host cation by a cation with a higher d-electron count or by oxygen deficiency. Bulk transport measurements show that for very slightly nonstoichiometric TiO$_2$ with a carrier concentration in the range below 2.0×10^{20} cm^{-3} the low-temperature activation energy for conduction is about 0.028 eV.[1] For more strongly reduced material a so-called type b activation energy is found that increases with increasing degree of reduction. This unusual behavior is attributed to an aggregation of point defects into shear planes with an enhanced trapping energy at shear plane sites. Obvious substitutional n-type dopants for TiO$_2$ are the group-V elements vanadium, niobium, and tantalum. These elements can be substitutionally incorporated within the rutile lattice to occupy at least 50% of the cation sites.[2–5] Indeed both VO$_2$ (Ref. 2) and NbO$_2$ (Refs. 3–5) form a complete range of solid solution with TiO$_2$. Nb doping gives rise to shallow donor states[6–9] 0.02–

0.03 eV below the conduction-band minimum and therefore at essentially the same energy as the donor states introduced by oxygen deficiency. By contrast, the states associated with V doping are much deeper in the bulk band gap: both photoemission[10,11] and photoperturbation of ESR (Refs. 12 and 13) reveal a vertical ionization energy for V-localized donor states of about 2.1 eV relative to the conduction-band minimum. The corresponding adiabatic energy that can be compared directly with transport measurements is 0.8 eV. Group V doping can in principle be electronically compensated by cation vacancies or oxygen interstitials whose equilibrium concentration increases dramatically with increasing oxygen fugacity. For V-doped TiO$_2$ it transpires that the degree of compensation is rather small,[10,11,14] even for samples equilibrated under atmospheric oxygen partial pressure. By contrast Nb-doped[15–17] and Ta-doped[18] TiO$_2$ are both much more susceptible to compensation.

Recent technological interest in Nb-doped TiO$_2$ derives from the fact that Nb doping leads to enhanced photocatalytic activity in the destruction of organochloride pollutants such as dichlorobenzene.[19] Nb doping in TiO$_2$ also produces a material with much enhanced catalytic activity in the reduction of NO by NH$_3$ (Ref. 20) and with an improved response in the sensing of O$_2$ and H$_2$.[21–23] The effects of Nb doping are generally attributed to the introduction of new

electronic states into the band structure of the parent material whose energy makes them accessible by thermal or photon excitation under the relevant conditions of the technological process.

The simple presumption that Nb doping introduces shallow donor states into TiO_2 at all doping levels was recently called into question by the growth of high-quality (100)- (Refs. 24–27) and (110)- (Refs. 25, 28 and 29) oriented single-crystal thin films of Nb-doped TiO_2 using oxygen-plasma-assisted molecular beam epitaxy. These films displayed excellent long-range order as gauged by low-electron energy diffraction (LEED) and reflection high-energy electron diffraction (RHEED), while it was demonstrated by photoelectron diffraction that the dopant Nb atoms occupied host Ti sites within the rutile lattice. Contrary to simple expectations, it was found that for doping levels between $x = 0.05$ and about $x = 0.40$ in material formulated as $Ti_{1-x}Nb_xO_2$, there was no indication in uv and x-ray excited photoemission spectra of new electronic states in the band gap of the TiO_2 host.[28,29] It was therefore postulated that Nb-induced states must overlap O $2p$ valence-band states. This is extremely surprising in view of the behavior of the system $Ti_{1-x}Nb_xO_2$ for limiting small and large values of x. At the lowest Nb-doping levels it is clear from the transport measurements alluded to above that the dopant introduces shallow donor levels just below the conduction-band minimum of the host material. At the other extreme, in NbO_2 itself experimental photoemission spectra demonstrate that there is a distinct Nb $4d$ band above the O $2p$ valence band.[30,31] Band-structure calculations on NbO_2 concur with this model and provide no clues as to why the $4d$ states in heavily-Nb-doped TiO_2 should be very much deeper in energy than in lightly doped material.[32]

Prompted in part by the surprising results of this recent work we report here a study of Nb-doped TiO_2 using high-resolution x-ray photoemission, variable photon energy resonance photoemission in the vacuum-uv regime, and scanning tunneling microscopy (STM). The photoemission spectra are considered in relation to cross-section-weighted density of states profiles for pure and Nb-doped TiO_2 clusters obtained from density-functional calculations. Most of the experimental work is carried out on ceramic polycrystalline material whose bulk oxygen stoichiometry can be precisely defined by a preparative procedure that reacts TiO_2 and NbO_2 in sealed quartz tubes. The study embraces the complete composition range in the system $Ti_{1-x}Nb_xO_2$ between $x = 0$ and $x = 1$. We have also studied TiO_2 single crystals doped to a low level by a diffusional technique. It is demonstrated that the conclusions to be drawn from the work on polycrystalline material are in accord with experiments on single-crystal samples.

II. EXPERIMENT

NbO_2 was prepared by reduction of Nb_2O_5 in flowing Ar/5% H_2 at 1200 °C. The material prepared in this way gave the x-ray powder diffraction pattern expected[33] for the room-temperature phase belonging to space group $I4_1/a$.[34] Samples of $Ti_{1-x}Nb_xO_2$ were prepared by reaction between an intimately ground mixture of NbO_2 and TiO_2 in evacuated and sealed quartz tubes. The required mixture was ground

together in an agate mortar and pestle and fired first at 650 °C for 1 day and then at 950 °C for 2 days. The mixture was then reground and refired at 1000 °C for a further 5 days. Finally the resulting material was formed into pellets by pressing between WC dies at 10 tonnes, and the resulting ''green bodies'' were sintered at 1000 °C in UHV (base pressure 10^{-10} mbar). Heating at this stage was achieved with the aid of a water-cooled copper work coil coupled to a 1.5-kW radio-frequency generator. Doped samples with x up to 0.6 gave simple powder x-ray diffraction patterns characteristic of a well-crystallized rutile phase. For $x = 0.8$ there was evidence of an onset of the crystallographic distortions, which lead to pairing of Nb atoms along the c axis in NbO_2 itself. The present observations are in accord with the phase diagrams proposed by Sakata[4] and Rüdorff and Luginsland[3] who reported onset of structural distortion around $x = 0.85$ and $x = 0.75$, respectively.

Single-crystal measurements were performed on (110)- and (210)-oriented single-crystal slices of TiO_2 (Pikem, Hereford, U.K.) that had been doped by a diffusional technique. A crystal slice of typical dimension 10 mm×10 mm×1 mm was packed in excess 1% Nb-doped TiO_2 powder prepared as above and sealed into an evacuated quartz ampoule. The crystals were then soaked in the doped powder at 1000 °C for 10 days. At the end of this time the crystals were extracted from the quartz tubes. To remove any loosely held sintered powder from the surface the crystals were polished with progressively finer diamond paste down to 1 μm using a water-based polishing fluid and were then rinsed ultrasonically in isopropanol and double distilled water.

High-resolution x-ray photoemission spectra were measured in a Scienta ESCA 300 spectrometer.[35] This incorporates a rotating-anode Al $K\alpha$ ($h\nu = 1486.6$ eV) x-ray source, a seven-crystal x-ray monochromator, and a 300-mm mean radius spherical sector electron energy analyzer with a parallel electron detection system. The x-ray source was run with 200-mA emission current and 14-kV anode bias, while the analyzer operated at 150-eV pass energy with 0.5-mm slits. Gaussian convolution of the analyzer resolution with a linewidth of 260 meV for the x-ray source gives an effective instrument resolution of 350 meV.

Ceramic pellets of Nb-doped TiO_2 and reference samples of Nb_2O_5 and NbO_2 were cleaned *in situ* in the preparation chamber of the Scienta spectrometer by annealing in UHV at about 750 °C for 2–3 h, heating being effected by an electron-beam heater. Doped and undoped (110)- and (210)-oriented single crystals were also studied in the Scienta spectrometer. Binding energies are referenced to the Fermi energy of an ion-bombarded silver foil that is regularly used to calibrate the spectrometer and should be accurate to ± 0.05 eV. There was no indication of sample charging during the x-ray photoelectron spectroscopy (XPS) measurements.

Vacuum-uv photoemission spectra of ceramic $Nb_{0.1}Ti_{0.9}O_2$ and NbO_2 were measured on beamline 6.2 of the synchrotron radiation source at the Daresbury Laboratory. This incorporated a monochromator with two sets of toroidal gratings covering the photon energy ranges 15–40 eV (710 lines/mm) and 40–140 eV (1800 lines/mm). The energy analyzer is housed in a chamber that achieved a base pressure of 2×10^{-10} mbar during the experimental run. The

analyser has 150° spherical sector deflection elements of mean radius 50 mm. Constant-initial-state (CIS) spectra were measured by scanning the analyzer synchronously with the high-energy monochromator to keep fixed on a constant initial state. For these scans the photon bandwidth was set at 0.5 eV. Count rates were normalized relative to the drain current from a tungsten mesh through which the beam passed just prior to hitting the sample. To construct the CIS curves the raw data were further corrected for the quantum efficiency of the beam monitor mesh, which had in turn been calibrated by measuring the drain current from a copper foil in the photoemission chamber as described in detail elsewhere.[36]

Finally STM measurements on diffusionally Nb-doped $TiO_2(110)$ were carried out in a commercial Omicron UHV STM operating at room temperature.[37] Electrochemically etched tungsten tips were used in all experiments. The STM is mounted in a UHV chamber with a base pressure of 4×10^{-11} mbar. The chamber was equipped with facilities for XPS and LEED. Annealing was performed by radiative heating on the rear side of the mount. The initial cleaning of the surface was achieved with repeated cycles of Ar-ion sputtering (1.4 kV, $10 \mu A$, 30 min) and annealing (700 °C, 20 min) until LEED patterns indicated a well-ordered (1×1) surface, and no impurities could be detected by XPS or STM imaging.

III. RESULTS

A. High-resolution x-ray photoemission of Nb_2O_5 and NbO_2

Valence-band photoemission spectra of Nb_2O_5 and NbO_2 are shown in Fig. 1, while corresponding Nb3d core-level spectra are shown in Fig. 2. The valence-band spectrum of Nb_2O_5 is dominated by a single broad feature associated with O2p states, although very weak structure is just visible close to the Fermi energy. This is derived from Nb4d states introduced by oxygen deficiency. The valence-band onset is at 3.45 ± 0.05 eV. This compares with a quoted bulk band gap of 3.41 eV.[38] Thus the photoemission data are consistent with a Fermi level pinned close to the conduction-band minimum by the donor states. The corresponding Nb3d core-level spectrum for Nb_2O_5 is shown in Fig. 2. The spectrum is basically a simple spin-orbit doublet with a Nb3$d_{5/2}$ binding energy of 207.8 eV relative to the Fermi level. An extremely weak low-binding-energy shoulder is apparent, presumably associated with the Nb(IV) arising from the oxygen vacancies. The lower panel of Fig. 1 shows the valence-band XPS of NbO_2. In addition to the valence-band peak, a sharp and well-defined peak appears close to the Fermi energy. This is associated with the Nb4d states of this $4d^1$ material.

NbO_2 adopts a distorted rutile structure[33,34,39,40] with a narrow homogeneity range at room temperature.[41] This phase is nonmetallic with an activation energy for conduction of 0.26 eV.[42] A transformation to an undistorted rutile phase takes place at 1070 K (Refs. 33, 34, and 40) with a large increase in conductivity suggestive of a nonmetal to metal transition.[42] Although earlier work described the transition to be first order, more recent neutron-diffraction studies suggest a second-order transition.[43] The nonmetallic behavior of the distorted room-temperature phase is best understood in terms of metal-metal bonding between Nb ions, which are paired along the c axis within the rutile struc-
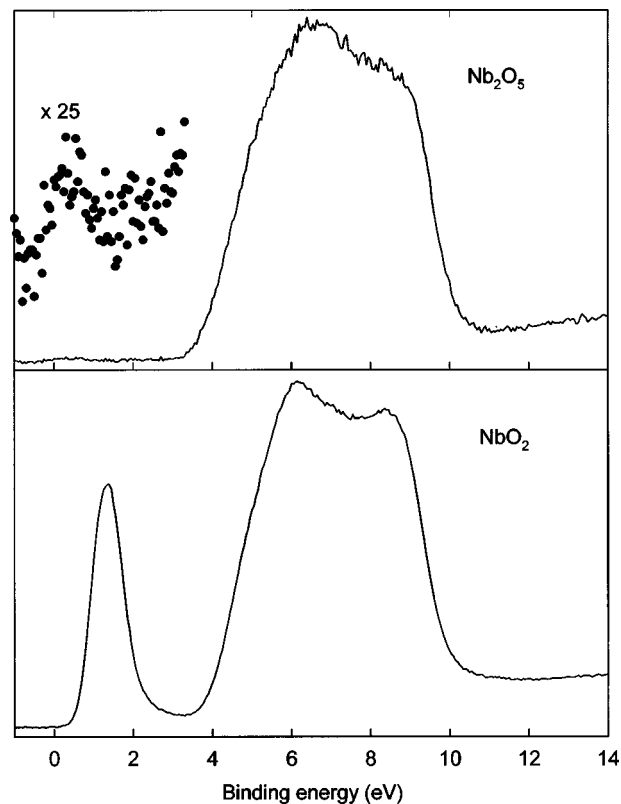

FIG. 1. Valence-band x-ray photoemission spectra of Nb_2O_5 and NbO_2. Binding energies are relative to the Fermi energy of a calibrant silver foil.

ture. This produces a splitting of the manifold of 4d bands to leave a lowest Nb-Nb σ-bonding band that can accommodate two electrons per pair of Nb ions. This band is therefore full in NbO_2, leading to the observed nonmetallic behavior.[42,44] The onset of the Nb 4d band in the experimental photoemission spectrum is 0.14 eV below the Fermi energy. Given the activation band gap of 0.26 eV alluded to above, the present data suggest that the Fermi level sits in the middle of the narrow gap produced by the room-temperature structural distortion.

The Nb 4d core-level spectrum of NbO_2 shown in Fig. 2 displays a complex core line shape, broadly in agreement with that reported earlier[45] given the improved resolution of the present work. The spectral structure is best interpreted in terms of final-state screening effects. Following Kotani and Toyazawa[46] and Wertheim and co-workers,[47,48] we recognize that ionization of a core level in a narrow-band metallic oxide[45] leads to a core-valence Coulomb interaction that may exceed the conduction-band width. In this situation the potential associated with the core hole will be sufficient to pull a localized level at the ionized site out of the metallic conduction band to produce a localized trap state. A ''well-screened'' final state is obtained if this trap level is occupied in the final state, but if the localized level remains empty a ''poorly screened'' final state is obtained. For a narrow band d^n oxide, the ''well-screened'' and ''poorly screened'' final states differ by one in their d-electron count. This model is readily extended to systems where structural distortion opens a small gap in the one-electron band structure, provided that the magnitude of the gap is much less than the core-valence
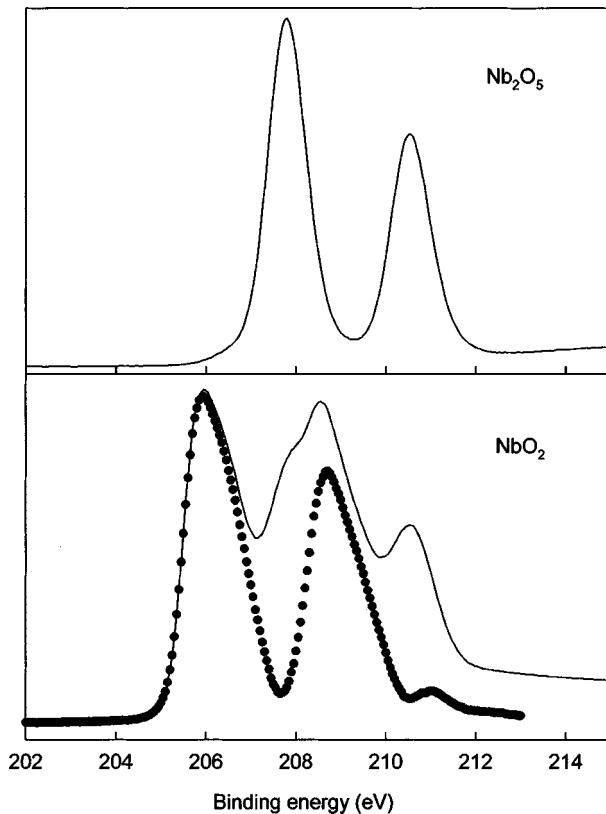
FIG. 2. Nb $3d$ core x-ray photoemission spectra of Nb_2O_5 and NbO_2. The dots in the lower panel spectrum of NbO_2 correspond to the contribution to the spectral signal from screened final states. This is obtained by subtraction of a suitably weighted background-subtracted Nb_2O_5 spectrum from the NbO_2 spectrum. Binding energies are relative to the Fermi energy of a calibrant silver foil.

Coulomb interaction. In the present case the binding energies of the spin-orbit components associated with poorly screened final state coincide with those found for Nb_2O_5, so that the poorly screened state corresponds to a $4d^0$ final-state configuration. The structure associated with the well-screened final-state configuration may be obtained simply by subtracting an appropriately weighted $4d^0$ spectrum from the composite spectral profile. This procedure leads to a clean spin-orbit doublet associated with the well-screened final state, aside from a weak peak to high binding energy that arises from subtle changes in the photoemission background. As expected from the Kotani model, the structure associated with the well-screened final state shows pronounced asymmetry in the line shape, reminiscent of the asymmetric Doniach-Sunjic line shape found for simple metals. The 0.26-eV threshold for electron-hole pair excitations in NbO_2 accentuates this asymmetry.

Despite the appeal of the physical model, the Kotani-Wertheim model has not gained total acceptance (especially in the catalytic literature) and there has been a recurring temptation to interpret core photoemission spectra of narrow-band metallic (or near-metallic) oxides in terms of the requirement that each distinct final-state d^n configuration must arise from a corresponding initial-state d^n configuration. This in turn leads to interpretation of complex spectral profiles in terms of contamination of the intrinsic material by ill-defined ‘‘surface phases’’ within which the oxidation state of the

metal cation differs from that of the parent bulk phase. Recent experiments[49] on single-crystal RuO_2 grown by molecular beam epitaxy (MBE) on $TiO_2(110)$ substrates revealed a complex Ru $4d$ spectral profile qualitatively similar to that for NbO_2. The screened and unscreened components of the complex core line showed the same azimuthal variations in intensity in a photoelectron diffraction experiment. This experiment provides a definitive demonstration that the photo-emitting atoms that give rise to the screened and unscreened peaks occupy identical crystallographic sites. The clear-cut situation with respect to the Ru $4d$ core line shape for RuO_2 gives us confidence in our interpretation of the complex line shape found for NbO_2 in terms of the Kotani-Wertheim model.

B. X-ray photoemission spectra of $Ti_{1-x}Nb_xO_2$

Valence-band photoemission spectra of the $Ti_{1-x}Nb_xO_2$ ceramics are shown in Fig. 3(a). Even at the lowest doping level a weak peak is apparent in the bulk band gap of the rutile host material. This peak grows in intensity monotonically with increasing doping level, converging on the intensity of the $4d$ peak found for NbO_2. The binding energy of the gap feature shows a small downward shift with increasing doping level. At 1% doping level, the peak maximum is at 0.8 eV. This is close to the vertical ionization energy of 1.0 eV for Ti $3d$ states in oxygen-deficient TiO_{2-x}.[50] At the highest Nb-doping level of 80% the peak maximum is at 1.40 eV binding energy, as found for NbO_2 itself. These findings accord with onset of the structural distortion that leads to Nb-Nb bonding at a doping level of around 80%. The oxygen valence-band onset energy also shows a progressive shift to high binding energy with Nb doping. For undoped TiO_2 the valence-band onset as gauged by a simple linear extrapolation of the valence-band edge is 3.08 ± 0.05 eV, in accord with the bulk band gap and a placement of the Fermi level very close to the conduction-band minimum. The increase of the binding energy of the O $2p$ onset with Nb doping then implies a widening of the bulk gap, an effect that can be understood in terms of stronger mixing between Nb $4d$ and O $2p$ states than between Ti $3d$ and O $2p$ states. As indicated previously the band gap for TiO_2 is smaller than that for Nb_2O_5.

The Nb $3d$ and Ti $2p$ core-level spectra corresponding to the valence-band spectra of Fig. 3 are shown in Figs. 4 and 5 respectively. The Nb $3d$ structure is presented with intensities scaled to the O $1s$ intensity. As expected, the absolute Nb $3d$ intensity increases with increasing doping level. However, there is also a striking evolution of the Nb $3d$ line shape from a simple spin-orbit doublet at low doping level toward the complex spectral profile of NbO_2 at the highest doping level. Figure 5 shows that there are also changes in the Ti $2p$ spectral profile with doping. The Ti $2p$ spectrum of nominally undoped vacuum annealed TiO_2 already has very weak low-binding-energy shoulders with about 2% of the intensity of the dominant spin-orbit doublet. These arise from Ti(III) states introduced by oxygen deficiency in the near-surface region probed by XPS. Since each oxygen vacancy introduces two donor $3d^1$ Ti(III) levels, the surface stoichiometry must be of the order $TiO_{1.99}$. The Ti(III) shoulders grow in intensity with increasing Nb doping. The Ti $2p$
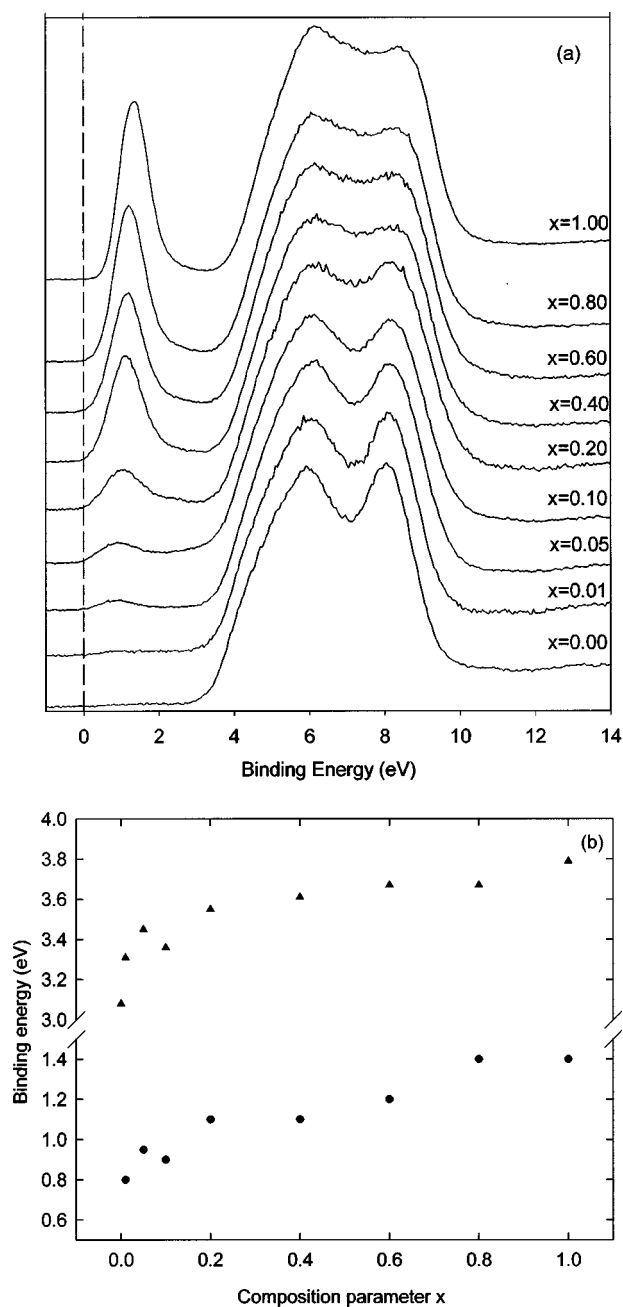
FIG. 3. (a) Valence-band x-ray photoemission spectra of $Ti_{1-x}Nb_xO_2$ ceramics for the differing x values indicated. Binding energies are relative to the Fermi energy of a calibrant silver foil. (b) Binding energy of the peak maximum for Ti $3d$ or Nb $4d$ photoemission feature in the bulk band gap (solid circles) and binding energy of the O $2p$ valence-band onset (solid triangles) for $Ti_{1-x}Nb_xO_2$ ceramics as a function of the composition parameter x.

FIG. 4. Nb $3d$ core-level x-ray photoemission spectra of $Ti_{1-x}Nb_xO_2$ ceramics for the differing x values indicated. Binding energies are relative to the Fermi energy of a calibrant silver foil. The absolute intensity is scaled relative to the intensity of the O $1s$ core level peak.

spectral profile is further complicated by the buildup of intensity to the high-binding-energy side of the doublet due to Nb $3s$ states.

The evolution of photoemission structure at low doping levels is further illustrated by curve fits to the spectral profiles in Fig. 6. At the lowest 1% doping level [Fig. 6(a)] the position of the Nb $3d$ doublet corresponds to that found in Nb_2O_5 so that the substitutional Nb is incorporated within the TiO_2 lattice as Nb(V). By contrast, even at this very low doping level there is a marked growth in intensity of the

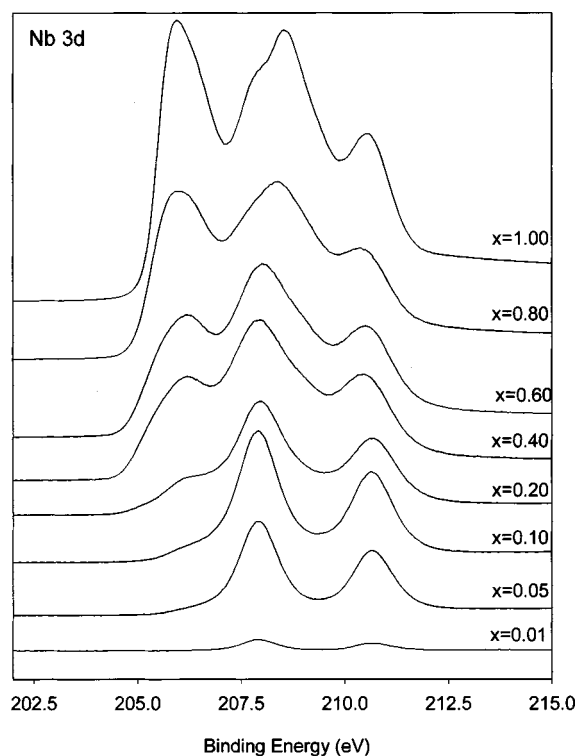Ti(III) structure. Thus the extra electrons introduced by Nb become transferred to Ti sites. The core photoemission spectra of Nb-doped TiO_2 contrast with those of V-doped TiO_2, which clearly show that the electron introduced by doping are trapped on V sites.[51] At 10% doping level [Fig. 6(b)], there is further growth in the intensity of the the Ti(III) structure but also development on shoulders on the low-binding-energy side of the Nb $3d$ doublet. These are due to Nb(IV).

The curve-fitting analysis may be used to quantify the distribution of excess charge between Ti and Nb and the degree of compensation at the surfaces of our UHV annealed ceramic samples. As shown in Fig. 7, the apparent surface concentration ratio [Nb]/{[Nb]+[Ti]} derived from cross-section-corrected Nb $3d$ and Ti $2p$ intensities increases with increasing doping level but is always higher than expected from the bulk doping level. This implies pronounced surface segregation of Nb in these samples, a not unexpected result given the larger size of Nb as compared with Ti. Size mismatch is one of the dominant thermodynamic driving forces for surface segregation in doped oxide systems.[52] In addition, the summed Ti(III) and Nb(IV) contribution to the overall cation core signal intensity is compared with the Nb content probed by XPS. In the absence of any compensation of the Nb doping, these two quantities should coincide. However as evident in Fig. 7 there is significant (but not complete) compensation for doping levels up to 20%. It was not possible to extend this analysis beyond low doping levels owing to the complexity in the line shapes at higher doping level (arising in part from overlap of Nb $3s$ structure with Ti $2p$ structure) and the complete breakdown in the relationship between the
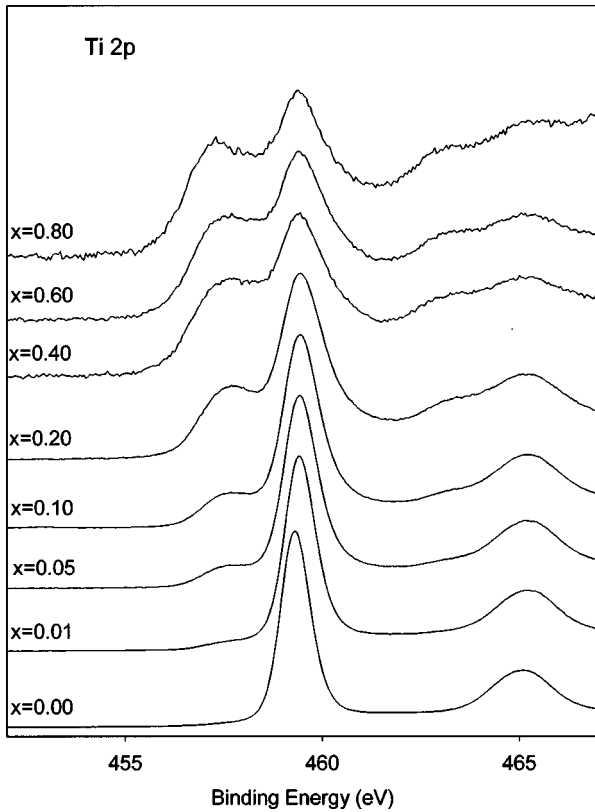
FIG. 5. Ti $2p$ core-level x-ray photoemission spectra of $Ti_{1-x}Nb_xO_2$ ceramics for the differing x values indicated. Binding energies are relative to the Fermi energy of a calibrant silver foil. The Ti $2p_{3/2}$ peak maximum is scaled to the same intensity in each spectrum.

final-state d^0:d^1 intensity ratio and the initial-state d-electron count for NbO_2. The charge distribution between Ti and Nb sites is also plotted in Fig. 7, revealing a significant transfer of charge back from Ti to Nb by the time 20% bulk doping has been achieved.

C. Resonance photoemission of band-gap states of $Ti_{0.9}Nb_{0.1}O_2$

Constant-initial-state photoemission profiles taken at 1 eV binding energy for $Ti_{0.9}Nb_{0.1}O_2$, oxygen-deficient TiO_{2-x}, and NbO_2 are shown in Fig. 8. The photon energy range between 30 and 50 eV embraces the Ti $3p$ and Nb $4p$ thresholds. The profile for TiO_{2-x} is reproduced from Ref. 53 and displays the well-known Fano line shape. This arises from interference between the direct photoemission channel,

$$Ti(3p^63d^1)+h\nu \rightarrow Ti(3p^63d^0)+e,$$
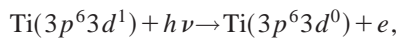
and a resonant channel involving $3p$ photoexcitation followed by super-Coster-Kronig decay:

$$Ti(3p^63d^1)+h\nu \rightarrow Ti(3p^53d^2)^*,$$

$$Ti(3p^53d^2)^* \rightarrow Ti(3p^63d^0)+e.$$
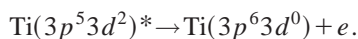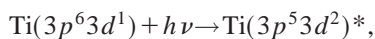
The Ti $3p$ core binding energy is about 37 eV, but the resonance edge reaches half its maximum height at a higher photon energy around 43.2 eV.

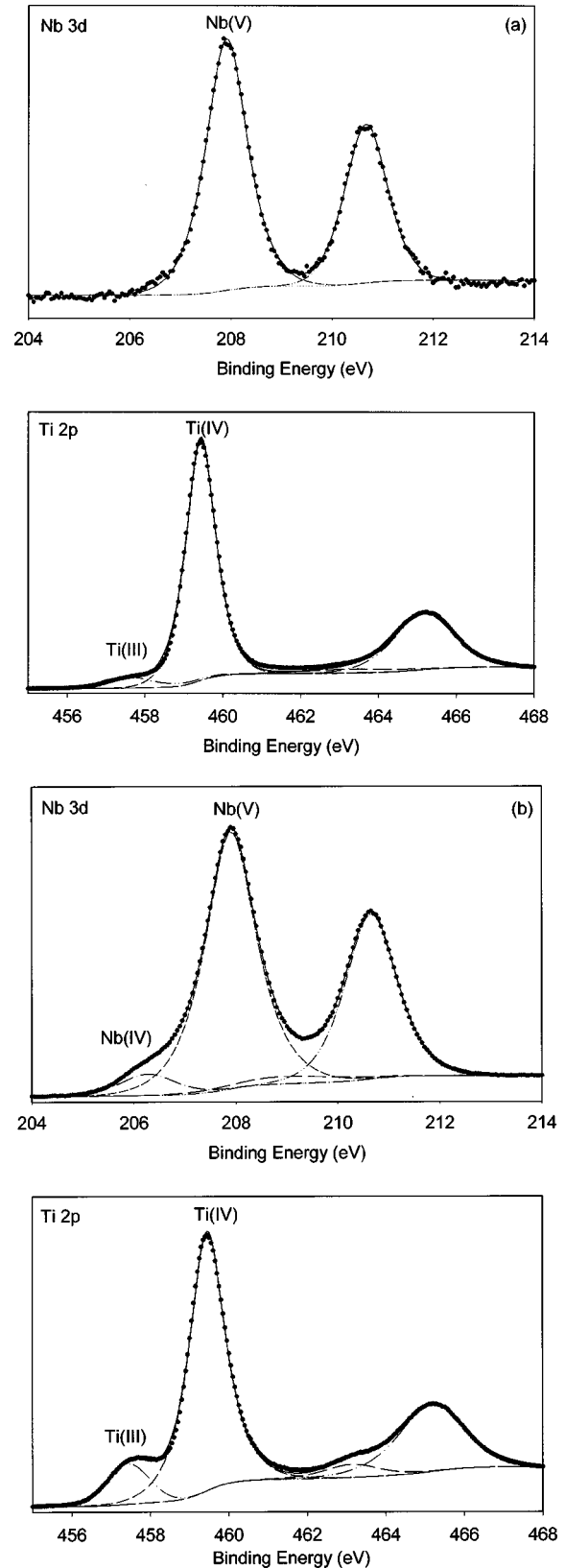FIG. 6. (a) Curve fit to the Nb $3d$ and Ti $2p$ core-level x-ray photoemission spectra of $Ti_{0.99}Nb_{0.01}O_2$ (1% Nb-doped TiO_2). (b) Curve fit to the Nb $3d$ and Ti $2p$ core-level x-ray photoemission spectra of $Ti_{0.90}Nb_{0.10}O_2$ (10% Nb-doped TiO_2). The dots are experimental data points and the solid lines are best fits to these data with an addition of a Shirley background and individual Voigt functions for Nb(V), Nb(IV), Ti(IV), and Ti(III) final states.
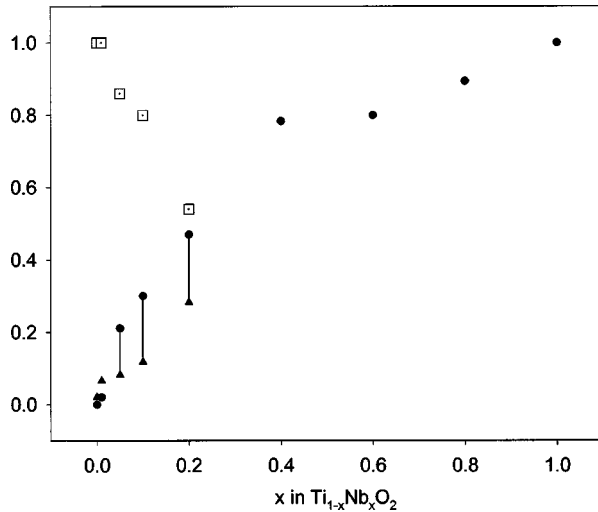
FIG. 7. Solid circles: the effective Nb cation site occupancy derived from core XPS. Solid triangles: the total fraction of cations in a reduced state. The solid lines linking the triangles to the circles indicate the degree of compensation $1-[n]/[\text{Nb}]$. Open squares: the distribution of the n-type carriers between Ti and Nb sites, i.e., $[\text{Ti(III)}]/[\text{Nb(V)}]$.

The Nb $4p$ core binding energy of NbO_2 is at the lower value 35 eV and the resonance profile now involves the interference between

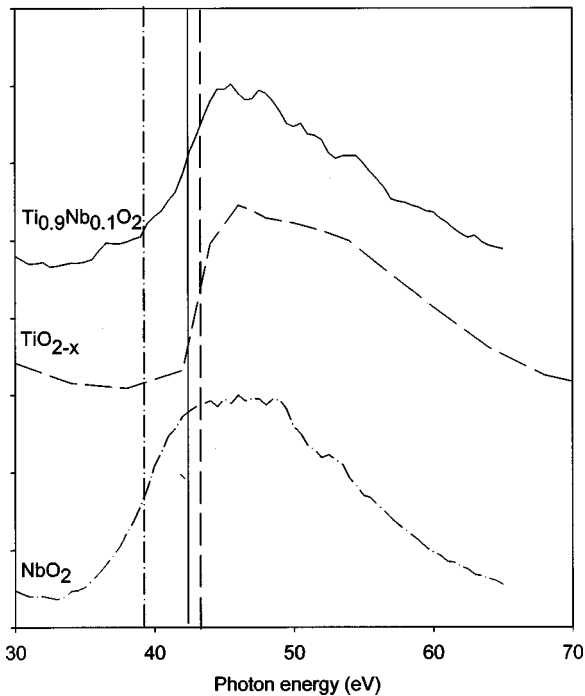$$\text{Nb}(4p^6 4d^1) + h\nu \rightarrow \text{Ti}(4p^6 4d^0) + e$$
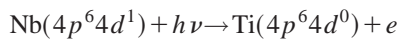
and

FIG. 8. Constant-initial-state resonant photoemission profiles taken at 1 eV binding energy for $\text{Ti}_{0.90}\text{Nb}_{0.10}\text{O}_2$ (solid curve), TiO_{2-x} (dashed curve), and NbO_2 (dash-dotted curve). The vertical lines identify the energy where the resonance edges reach half of maximum intensity.
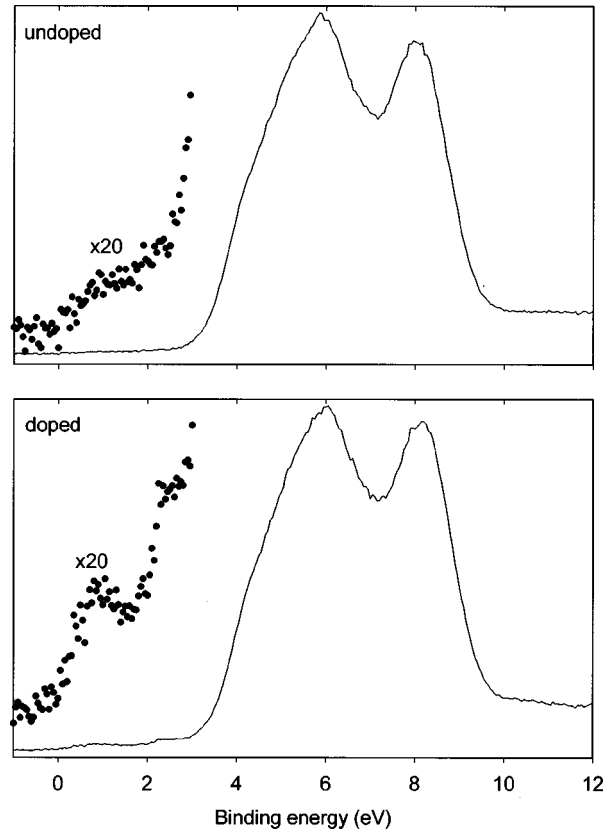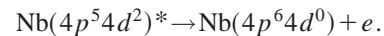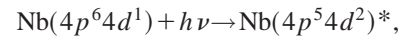

FIG. 9. Valence-band XPS of undoped TiO_2(110) (upper spectrum) and TiO_2(110) doped with Nb by diffusion from 1% Nb-doped TiO_2 powder (lower spectrum).

$$\text{Nb}(4p^6 4d^1) + h\nu \rightarrow \text{Nb}(4p^5 4d^2)^*,$$

$$\text{Nb}(4p^5 4d^2)^* \rightarrow \text{Nb}(4p^6 4d^0) + e.$$

The resonance edge for NbO_2 reaches half maximum height at 39.2 eV photon energy. The resonance profile for the doped system is characterized by a resonance edge reaching half-maximum height at 42.5 eV photon energy. As is clear from Fig. 8 this is much closer to the value for TiO_{2-x} than for NbO_2. Resonance photoemission thus reinforces the conclusion that at low doping level the electrons associated with the band-gap state reside mainly on Ti. Again the results of the present study contrast with those for V-doped TiO_2,[54] where the resonance edge of the dopant-induced gap peak coincides with that for VO_2 (Ref. 55) rather than TiO_{2-x} (Ref. 53). Thus resonant photoemission confirms the conclusion from core photoemission that the trapping site for n-type donor electrons differs between the two dopant systems.

D. X-ray photoemission, STM, and LEED observations on diffusion-doped TiO_2 single crystals

Both (110)- and (210)-oriented[56] single crystals of TiO_2 diffusionally doped from 1% Nb-doped rutile were studied by high-resolution x-ray photoemission, with essentially similar results. As shown in Fig. 9, Nb doping leads to enhanced photoemission intensity in the rutile band gap. This is associated with increased intensity of the low-binding-energy shoulder associated with Ti(III) in core-level photoemission (Fig. 10). In this case the increase in the $[\text{Ti(III)}]/$
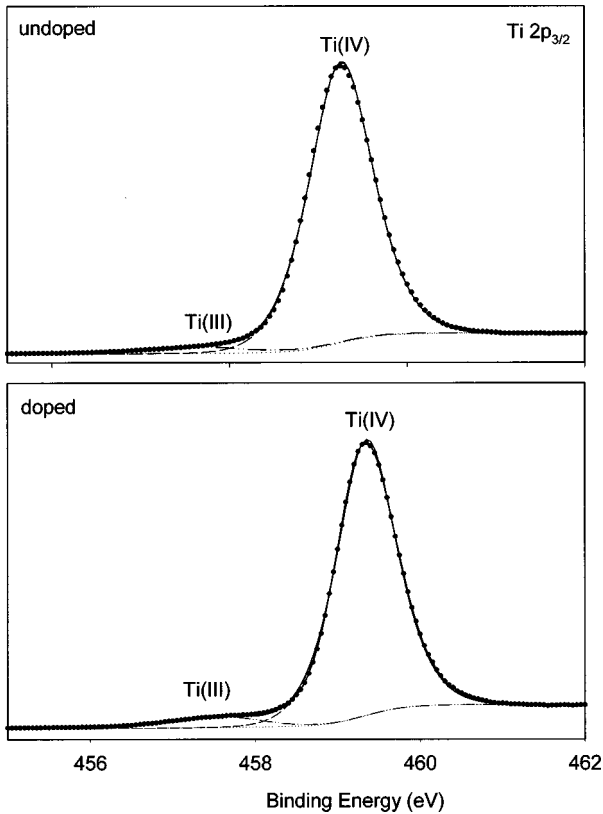
FIG. 10. Ti $2p_{3/2}$ core XPS of undoped $TiO_2(110)$ (upper spectrum) and $TiO_2(110)$ doped with Nb by diffusion from 1% Nb-doped TiO_2 powder (lower spectrum).

[Ti(total)] ratio from 0.035 to 0.057 is close to the Nb-doping level $[Nb]/\{[Nb]+[Ti(total)]\}=0.016$ inferred from the Nb $3d$ intensity. Moreover, as with the ceramic samples, the Nb core line is characteristic of Nb(V). Thus the behavior of single-crystal Nb-doped TiO_2 is in line with that found for ceramic samples at comparably low doping levels.

Typical LEED patterns from a (110)-oriented Nb-doped crystal are shown in Fig. 11. There is no indication of dopant ordering and the pattern corresponds to the well-known (1×1) reconstruction for $TiO_2(110)$. An STM image from the doped crystal is shown in Fig. 12. This was obtained at +2.0 V sample bias and 1 nA tunnel current, i.e., under conditions where the STM imaging probes contours of empty state charge density. The image is dominated by bright rows running along the [001] direction, as observed in many previous studies.[57-62] In addition the image contains a number of "extra bright" clusters. Some of these are resolved into a square of four "extra bright" spots appearing on the bright rows.

The electrostatically stable[63] (1×1) reconstruction of $TiO_2(110)$ involves two Ti ions per surface unit cell. Half of the surface Ti ions are coordinated by only five oxygen ions. However, rows of bridging oxygen ions running along the [001] direction that comprise the outer {O} layer lie above the surface Ti_2O_2 plane and complete the sixfold coordination of the remaining surface Ti ions. STM images of $TiO_2(110)$ obtained at positive sample bias contain bright rows aligned parallel to [001]. The rows in STM could correspond either to the bridging oxygen rows or to the rows of bare fivefold-coordinated Ti ions. On the basis of experiments involving adsorption of formate[64] or chlorine[65] the

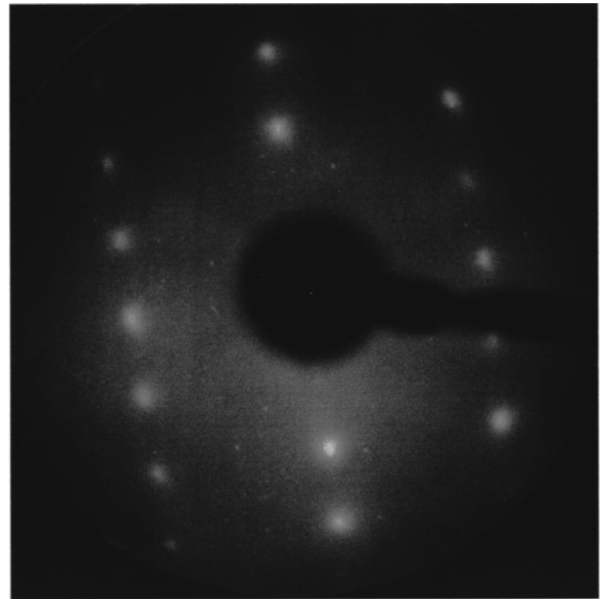FIG. 11. LEED pattern of Nb-doped $TiO_2(110)$ taken at 95 eV beam energy.

latter interpretation is now favored. Density-functional calculations reveal that contours of empty-state charge-density bend outward above Ti positions more strongly than above O positions, even though the bridging O ions are uppermost.[66] Thus electronic structure effects dominate purely structural effects in determining the form of STM images.

Within this interpretation of STM images for TiO_2 itself, we then associate each "extra bright" cluster with Ti ions surrounding a single Nb dopant atom at the surface. The Nb(V) dopant species are presumed to occupy sites between the bright rows. Charge transfer to the surrounding Ti ions then yields gray-scale contrast in the STM images: the en-
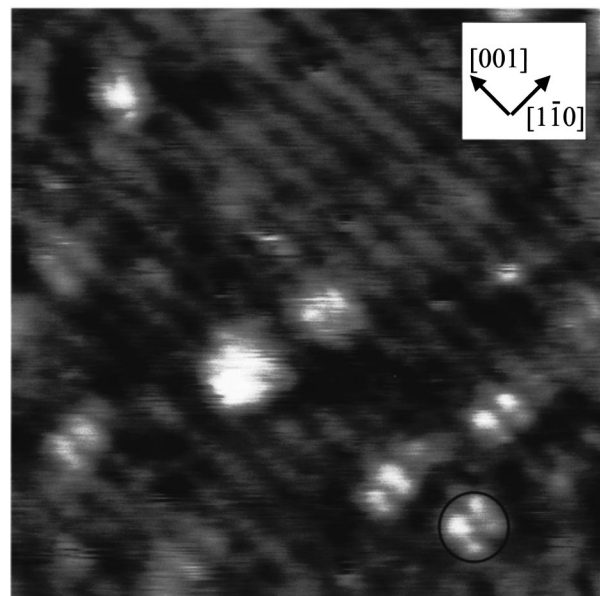

FIG. 12. $100\,\text{Å} \times 100\,\text{Å}$ STM image of Nb-doped $TiO_2(110)$ acquired at 1 nA tunnel current and +2.0 V sample bias. A single bright spot cluster (which is believed to correspond to a Nb-dopant atom) is highlighted with a circle.

hanced brightness is most easily understood in terms of increased local conductivity. The separation of the spots within the cluster of about 6 Å along the [001] direction is somewhat surprising as this distance is twice the separation between Ti ions along [001]. If the Nb ions occupied sixfold-coordinated sites in the surface ionic layer we would expect symmetric delocalization of charge to either side along the [001] direction, thus giving clusters with a spot separation of 3 Å (or 9 Å if the delocalization extended over three surface unit cells). One simple model that accounts for delocalization over two cells involves preferential incorporation of dopant atoms within the subsurface Ti_2O_2 layer in the Ti sites under the bridging oxygen rows. The Ti sites in this layer are displaced by half a unit cell along the [001] direction relative to Ti sites in the topmost Ti_2O_2 layer. Symmetric delocalization of charge onto adjacent Ti ions including those in the topmost Ti_2O_2 layer would naturally encompass two surface unit cells.

The STM image of Fig. 11 has a total area of 10^4 Å^2 and includes 1040 cation sites. Given that the surface Nb concentration probed by XPS is 1.1%, we expect to see about 11 clusters in this image. We used an automated image analysis program to count bright clusters with dimensions of $(6 \pm 1)^2$ Å^2 in a large number of images encompassing a total area of 2.76×10^7 Å^2, i.e., 276 times the area depicted in Fig. 12. We find the mean number of clusters per 10^4 Å^2 is 7. This is somewhat lower than expected from XPS, although of course XPS measures the average Nb concentration over a range of atomic layers within the effective probing depth of the technique and not simply the concentration in a single atomic layer.

IV. DISCUSSION

A. Comparison with previous experimental work

The as-prepared Nb-doped TiO_2 ceramics studied in the present work were all intensely blue or blue-black materials, while the diffusionally doped single crystals displayed a deep blue coloration similar to that found for TiO_2 crystals reduced by annealing in hydrogen. This accords with previous work which found a band at 1 eV in diffuse reflectance spectra whose intensity increased with increasing doping Nb doping level.[67] Undoped TiO_2 ceramics or crystals developed a much less intense coloration as a result of annealing in UHV and displayed essentially no color change after annealing is sealed quartz tubes. These simple observations suggest that doping is associated with the introduction of new electronic states into the host band gap, giving rise to new optical excitation processes in the visible region. In accord with this expectation distinct photoemission features are found in the bulk band gap and there is a sensible evolution of electronic properties between the TiO_2 and NbO_2 end members.

The present findings are thus at variance with work on Nb-doped TiO_2 films grown by deposition of Ti and Nb metal in an oxygen radical plasma. In that work the epitaxial material was formulated as $Ti_{1-x}Nb_xO_2$, but no photoemission features were found in the host band gap.[28,29] Moreover, the films were reported to be optically transparent in the visible region and exhibited poor electrical conductivity. It is therefore interesting to consider the likely degree of compensation under the conditions of MBE growth. The bulk defect

chemistry of Nb-doped TiO_2 was investigated in detail by Tani and Baumi,[18] who considered the dependence on oxygen partial pressure of the titanium interstitial concentration $[Ti_i^4]$, the titanium cation vacancy concentration $[V_{Ti}^4]$ and the n-type and p-type carrier concentrations, designated n and p. The interrelationships between these quantities are governed by three quasichemical equilibrium constants:

$$K_1 = [Ti_i^4]n^4 P(O_2), \tag{1}$$

$$K_2 = [V_{Ti}^{4'}]p^4 / P(O_2), \tag{2}$$

$$K_3 = np. \tag{3}$$

Charge balance requires that

$$[Nb_{Ti}] + 4[Ti_i^4] + p = n + 4[V_{Ti}^{4'}], \tag{4}$$

where $[Nb_{Ti}]$ is the substitutional Nb-doping concentration. The n-type carrier concentration is in turn determined by the nonlinear equation:

$$4K_1 / \{n^4 P(O_2)\} + [Nb_{Ti}] = n + 4K_2 K_3^{-4} n^4 P(O_2). \tag{5}$$

Values for the constants K_1 and the product $K_2 K_3^{-4}$ were determined from conductivity measurements taken in the range up to 1623 K. The term $4K_1 / \{n^4 P(O_2)\}$ is only important at exceedingly low oxygen partial pressures or low niobium-doping levels and accounts for the introduction of donor states by completely ionized titanium intersitials. Thus in the regime of relevance to oxygen plasma assisted MBE growth n depends on the simplified relationship:

$$4K_2 K_3^{-4} n^4 p(O_2) + n - [Nb_{Ti}] = 0. \tag{6}$$

At sufficiently low oxygen partial pressure $n = [Nb_{Ti}]$, and the Nb doping is uncompensated. However, at higher oxygen partial pressure the concentration of compensating cation vacancies increases and the carrier concentration drops off with oxygen partial pressure essentially according to the relationship

$$n = \{[Nb_{Ti}]K_3^4 K_2^{-1} / 4p(O_2)\}^{1/4}. \tag{7}$$

Making a logarithmic extrapolation versus inverse temperature for the values for $K_2 K_3^{-4}$ tabulated by Tani and Baumi we estimate that at 873 K (the temperature of MBE growth), $K_2 K_3^{-4} = 10^{-49}$. It is then possible to solve Eq. (5) for various doping levels and oxygen partial pressures. Taking specific values relevant to the MBE growth conditions of $p(O_2) = 5 \times 10^{-5}$ torr (which is equivalent to 6.6×10^{-8} atm) and $[Nb_{Ti}] = 3.2 \times 10^{21}$ cm^{-3} (corresponding to occupation of 10% of Ti sites by Nb), we obtain $n = 1.87 \times 10^{19}$ cm^{-3}. Thus the concentration of occupied donor states is only 0.58% of the Nb-doping level and the remaining 99.42% of the Nb doping needs to be compensated in some way. This would require vacancies on 2.48% of the cation sites or (less likely) oxygen interstitials. The n-type

carrier concentration is the same as would be found in uncompensated $Ti_{0.9994}Nb_{0.0006}O_2$ and would be difficult to observe in photoemission. This simple calculation assumes that the effective oxygen fugacity in the plasma corresponds simply to the background oxygen pressure. In practice the plasma is likely to be even more strongly oxidizing so that the degree of compensation could well be greater. Thus under the conditions of MBE growth most of the Nb dopant and the host Ti should be in their maximal oxidation state, i.e., we have Ti(IV) and Nb(V). Interestingly it appears that the stability range for the Nb-doped rutile phase under the oxidising conditions of MBE growth is much greater than for bulk material. When $Ti_{1-x}Nb_xO_2$ is oxidized the phase diagram for the TiO_2/Nb_2O_5 system[68] indicates that the monoclinic phase $TiNb_2O_7$ exsolves[69] when the Nb-doping level exceeds about 8%. In the MBE experiments compensated Nb can be incorporated within the rutile phase for TiO_2 doping levels up to 40%.

We need next to consider whether the conclusion that Nb is oxidized to Nb(V) in the oxygen plasma can be reconciled with the Nb $3d_{5/2}$ binding energy of 206.96 eV reported for the doped films.[28,29] Due to charging problems absolute binding energies could not be obtained. Instead a tabulated value[70] of 458.7 eV for the Ti $2p_{3/2}$ binding energy in TiO_2 was used as reference and the experimental Nb $3d_{5/2}$ binding energy was shifted accordingly. In the present work we find the Ti $2p_{3/2}$ binding energy for TiO_2 to be 459.30 ± 0.05 eV and the Nb $3d_{5/2}$ binding energy of Nb_2O_5 to be 207.80± 0.05 eV. Thus the difference between the Ti $2p_{3/2}$ and Nb $3d_{5/2}$ binding energies of $(458.7 - 206.96)$ eV $=251.74$ eV found in the earlier work compares with a value of $(459.30 - 207.80)$ eV$=251.5$ eV for the difference between Ti(IV) in TiO_2 and Nb(V) in Nb_2O_5 found in the present work. The discrepancy of 0.24 eV is barely significant and in further reduced to 0.09 eV if we use a more appropriate Ti(IV) $2p_{3/2}$ binding energy of 459.45 ± 0.05 eV for Ti in Nb-doped TiO_2 with doping levels in excess of 5%.

The extreme susceptibility of the Nb-doped TiO_2 system to compensation probably accounts for the discrepancy between the effective donor level to be inferred from our core photoemission measurements and the Nb-doping level. Thus again considering 10% Nb-doped material with $[Nb_{Ti}]=3.2 \times 10^{21}$ cm^{-3}, the n-type donor level is reduced to $[Nb_{Ti}] = 1.6 \times 10^{21}$ cm^{-3} (i.e., there is 50% compensation) if the surface is equilibrated with an oxygen partial pressure of 4.6×10^{-9} torr at 750 °C. This is well above the residual oxygen partial pressure in the vacuum systems we have used. However at 600 °C, the critical pressure for 50% compensation is 4.6×10^{-13} torr. We had no means of monitoring oxygen partial pressure at this low level and we cannot guarantee that the critical pressure is not exceeded. Thus even though the equilibrium degree of compensation at the annealing temperature of 750 °C should ensure minimal compensation, if the surface equilibrates with the residual oxygen background pressure during cooling from 750 °C, there may be significant (but not complete) compensation provided that sufficient ionic mobility is retained during sample cooling.

Finally we consider the present evidence for electron trapping on Nb rather than Ti sites at low doping levels in relation to previous experimental work. X-ray absorption measurements on both ceramic[71,73] and thin-film[72] TiO_2-NbO_2 solid solutions are consistent with formulation of material with a low Nb-doping level as $Ti(IV)_{1-2x}Ti(III)_xNb(V)_xO_2$ rather than $Ti(IV)_{1-x}Nb(IV)_xO_2$. An analogous situation pertains for Ta doped material.[74] This conclusion is further supported by ESR measurements.[67]

B. Comparison with cluster calculations

The valence-band XPS obtained in present work may be compared with density-of-states profiles for Nb-doped Ti oxide clusters calculated by the density-functional method (DF) within the local density approximation as parametrized by Vosko, Wilck, and Nusair.[75] The approach used has been described in detail elsewhere[76] and involves elimination of unwanted dangling bond states with the use of pseudohydrogen saturators. This technique satisfactorily describes structural and electronic properties of oxides and their surfaces,[77,78] including TiO_2.[79,80] In the present case we consider a cluster introduced earlier[76] containing 13 Ti ions and 45 O ions. This cluster contains a row of five of the fivefold coordinated Ti ions found on TiO_2(110) and two rows of four sixfold coordinated Ti ions on the same surface. The dangling bonds on O ions at the edges of the cluster that are unsaturated in comparison with TiO_2(110) are terminated with the appropriate number of hydrogen saturators.[76] This procedure gives an electrostatically neutral cluster.

Density-of-states profiles were obtained by broadening the pattern of discrete cluster eigenvalues with a Lorentzian of 0.3 eV half width. Partial densities of states for direct comparison with experiment were then obtained by decomposing each cluster level into its atomic contributions and weighting the contribution from different types of atomic orbital with one electron ionization cross sections appropriate to Al $K\alpha$ radiation.[81] Only O atoms not carrying a saturator were included in this summation, and the weighting was adjusted to ensure that the two different sorts of Ti and O ion at the TiO_2(110) surface made equal contribution to the cross-section-weighted density of states.

Figure 13(a) shows cross-section-weighted densities of states for a pure Ti-containing cluster and for a cluster containing a single Nb ion. The latter corresponds to an effective Nb:Ti ratio of 1/9 and should bear direct comparison with x-ray photoemission data for $Nb_{0.1}Ti_{0.9}O_2$. In agreement with the experimental observations a distinct new state appears above the O $2p$ valence band as a result of Nb doping. The separation between this new level and the main O $2p$ "valence band" is less than observed experimentally. This appears to be a general failure of local-density approximation (LDA) methods, which in both periodic and cluster calculations tend to underestimate band gaps. The atomic nature of the band-gap state is revealed in Fig. 13(b), which shows the Nb $4d$ and Ti $3d$ partial density of states for the Nb-doped cluster. The gap state has mixed Ti $3d$/Nb $4d$ character. Qualitatively this is in agreement with experiment, although the Ti $3d$/Nb $4d$ ratio is somewhat lower than implied by core-level spectra. The partial density-of-states plots also reveal that there is a pronounced Ti $3d$ and Nb $4d$ contribution to states in the valence band, which have predominant O $2p$ character. This arises from strong O $2p$–metal d covalency.
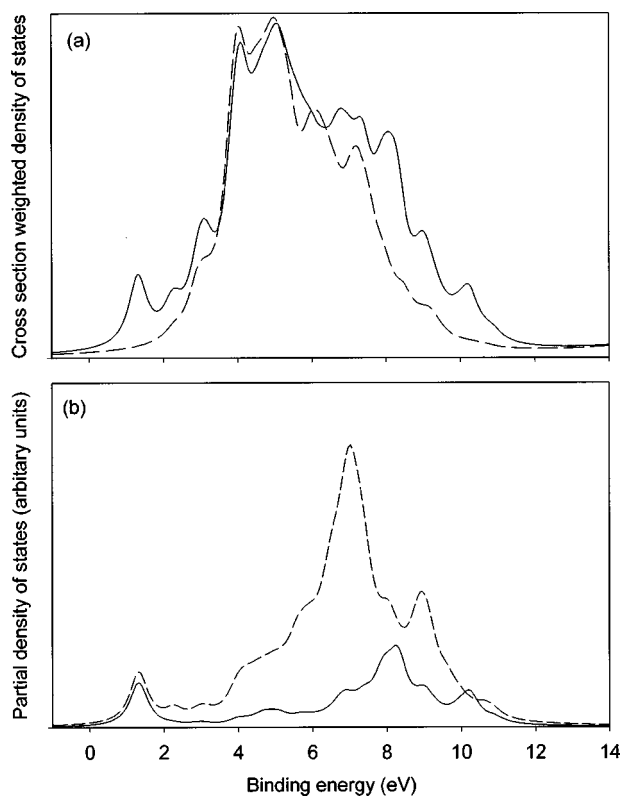
FIG. 13. (a) Cross-section-weighted density-of-states profiles for clusters designed to mimic TiO_2. Solid line is for cluster containing only Ti cations. Dashed line is for cluster containing a single Nb ion. The density-of-states (DOS) profile for the latter corresponds essentially to $Ti_{0.9}N_{0.1}O_2$. (b) Unweighted partial densities of states for the Nb-doped cluster. Solid line is Nb $4d$ partial DOS-dashed line Ti $3d$ partial DOS.

The relative metal d contribution is strongest in the states toward the bottom of the valence band.

A striking feature of the cross-section-weighted density of states profiles is the increase in spectral weight toward the bottom of the valence band arising from Nb doping. This arises from the metal oxygen hybridization discussed above and the fact that the one electron cross section for ionization of Nb $4d$ states ($\sigma = 8.7 \times 10^{-4}$ Mb) is at least an order of magnitude larger than for ionization of Ti $3d$ ($\sigma = 8.5 \times 10^{-5}$ Mb) or O $2p$ ($\sigma = 6.0 \times 10^{-5}$ Mb) states.[81] The consequences of this effect are further explored in Fig. 14 where the theoretical photoemission difference spectrum between the Nb-doped and the undoped cluster are compared with the experimental difference spectrum between $Nb_{0.1}Ti_{0.9}O_2$ and undoped TiO_2. The latter reveals a pronounced increase in intensity across the O $2p$ band as well as growth of the gap peak. It should be emphasised that the increased intensity in the O $2p$ valence band does not arise from the introduction of new states into this region but merely from a change in the atomic character of the states.

V. CONCLUDING REMARKS

Valence-band photoemission spectra of Nb-doped TiO_2 reveal a new state in the band gap of the rutile host material whose intensity increases with increasing doping level. Core-level spectroscopy and resonant photoemission demon-
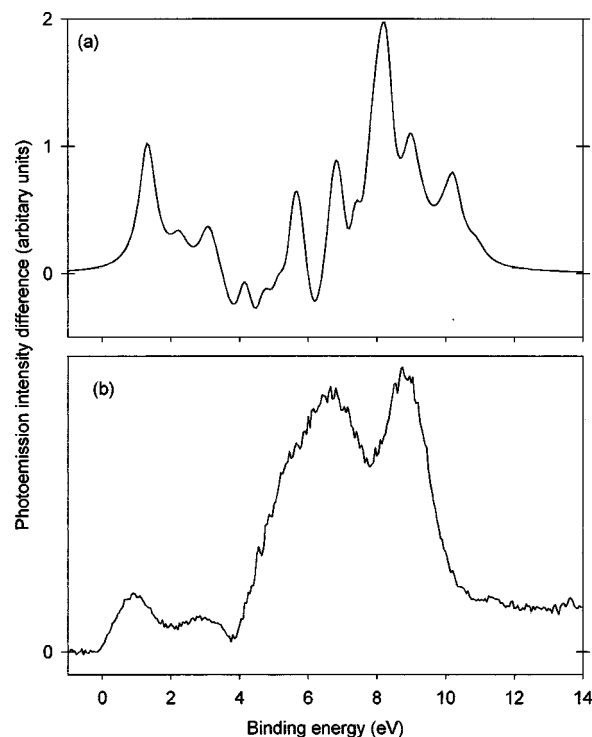

FIG. 14. (a) Theoretical photoemission difference spectrum between the Nb-doped and undoped cluster. (b) Experimental x-ray photoemission difference spectrum between $Ti_{0.9}N_{0.1}O_2$ and TiO_2. Intensities have been normalized relative to the O $2s$ band.

strate that at low doping level the extra electrons associated with Nb doping are localized mainly on Ti rather than Nb, so the lightly doped material is better formulated as $Ti(IV)_{1-2x}Ti(III)_x Nb(V)_x O_2$ rather than $Ti(IV)_{1-x}Nb(IV)_x O_2$. The present photoemission measurements thus concur with conclusions drawn from a broad range of techniques including x-ray absorption spectroscopy (XAS),[71–73] ESR, optical spectroscopy,[67] and transport measurements.[6–9] However, our conclusions differ from those inferred from work on Nb-doped TiO_2 grown by oxygen-plasma-assisted MBE.[28,29] Here x-ray photoemission spectra in material formulated as $Ti_{1-x}Nb_x O_2$ ($0.1 < x < 0.4$) were free of new states in the bulk band gap but the photoemission intensity increased across the O $2p$ valence band. This led to the proposal that the new Nb $4d$ states overlap the O $2p$ valence-band states and are therefore very much ''deeper'' than expected from transport measurements on very lightly doped TiO_2. However, consideration of the oxygen pressure during MBE growth leads us to believe that oxidation of Nb(IV) is inevitable under the growth conditions so that the Nb dopant is present as Nb(V) compensated by cation vacancies (or perhaps oxygen interstitials). Cluster calculations revel that there is significant Nb-O covalency in the both doped-uncompensated and doped-compensated material,[76] which O introduces Nb $4d$ character into the $2p$ valence-band states. The cross section for ionization of Nb $4d$ states is very much bigger than the cross section for ionization of Ti $3d$ or O $2p$ states, and the increased valence-band intensity that arises from Nb doping is easily rationalized within the framework of a simple Gelius-type model.

Comparison of the present results for Nb-doped TiO_2 with

earlier work on V-doped TiO_2 reveal a simple qualitative difference between the two systems: in the V-doped material electrons are trapped on the dopant atom rather than on host cation sites.[10,11] This difference may be ultimately traced to the differing Coulomb potentials associated with the two differing dopant atoms.

*Corresponding author. Electronic address: russ.egdell@chem.ox.ac.uk

[1] *Semiconductors: Physics of Non-Tetrahedrally Bonded Binary Compounds III*, edited by O. Madelung, Landolt-Bornstein, New Series, Group III, Vol. 17, Pt. g (Springer Verlag, Berlin, 1984).

[2] B. O. Marinder and A. Magneli, Acta Chem. Scand. **12**, 1345 (1958).

[3] W. Rüdorff and H.-H. Luginsland, Z. Anorg. Allg. Chem. **334**, 125 (1964).

[4] K. Sakata, J. Phys. Soc. Jpn. **26**, 1067 (1969).

[5] K. Sakata, I. Nishida, M. Matsushima, and T. Sakata, J. Phys. Soc. Jpn. **27**, 506 (1969).

[6] P. F. Chester, J. Appl. Phys. **32**, 866 (1961).

[7] M. Itakura, N. Nizeki, H. Toyoda, and H. Iwasaki, Jpn. J. Appl. Phys. **6**, 311 (1967).

[8] J. W. DeFord and O. W. Johnson, J. Appl. Phys. **54**, 889 (1983).

[9] T. Okamura and H. Okushi, Jpn. J. Appl. Phys., Part 2 **32**, L454 (1993).

[10] A. E. Tavener, C. Rayden, S. Warren, A. Gulino, P. A. Cox, and R. G. Egdell, Phys. Rev. B **51**, 6833 (1995).

[11] R. G. Egdell, A. Gulino, C. Rayden, G. Peacock, and P. A. Cox, J. Mater. Chem. **5**, 499 (1995).

[12] K. Mizushima, M. Tanaka, and S. Iida, J. Phys. Soc. Jpn. **32**, 1519 (1972).

[13] K. Mizushima, M. Tanaka, A. Asai, S. Iida, and J. B. Goodenough, J. Phys. Chem. Solids **40**, 1129 (1979).

[14] A. Vejux and P. Courtine, J. Solid State Chem. **23**, 93 (1978).

[15] J. F. Baumard and E. Tami, J. Chem. Phys. **67**, 857 (1977).

[16] N. G. Eror, J. Solid State Chem. **38**, 281 (1981).

[17] J-F. Marucco, B. Poumellec, J. Gautron, and P. Lemasson, J. Phys. Chem. Solids **46**, 709 (1985).

[18] E. Tani and J. F. Baumi, J. Solid State Chem. **32**, 105 (1980).

[19] H. Cui, K. Dwight, S. Soled, and A. Wold, J. Solid State Chem. **115**, 187 (1995).

[20] S. Okazaki and T. Okuyama, Bull. Chem. Soc. Jpn. **56**, 2159 (1983).

[21] K. Zakrzewska, M. Radecka, and M. Rekas, Thin Solid Films **310**, 161 (1997).

[22] M. Z. Atashbar, H. T. Sun, B. Gong, W. Wlodarski, and R. Lamb, Thin Solid Films **326**, 238 (1998).

[23] R. K. Sharma, M. C. Bhatnagar, and G. L. Sharma, Appl. Surf. Sci. **92**, 647 (1996).

[24] S. A. Chambers, Y. Gao, S. Thevuthasan, Y. Liang, N. R. Shivaparan, and R. J. Smith, J. Vac. Sci. Technol. A **14**, 1387 (1996).

[25] Y. Gao and S. A. Chambers, J. Mater. Res. **11**, 1025 (1966).

[26] S. Thevuthasan, N. R. Shivaparan, R. J. Smith, Y. Gao, and S. A. Chambers, Appl. Surf. Sci. **115**, 381 (1997).

[27] Y. Gao, Y. Liang, and S. A. Chambers, Surf. Sci. **365**, 638 (1996).

[28] Y. Gao, Y. Liang, and S. A. Chambers, Surf. Sci. **348**, 17 (1996).

[29] S. A. Chambers, Y. Gao, Y. J. Kim, M. A. Henderson, S. Thevuthasan, S. Wen, and K. L. Merkle, Surf. Sci. **365**, 625 (1996).

[30] G. Thornton, A. F. Orchard, and C. N. R. Rao, Phys. Lett. **54A**, 235 (1975).

[31] N. Beatham and A. F. Orchard, J. Electron Spectrosc. Relat. Phenom. **16**, 77 (1979).

[32] J. H. Xu, T. Jarlborg, and A. J. Freeman, Phys. Rev. B **40**, 7939 (1989).

[33] T. Sakata, K. Sakata, and I. Nishida, Phys. Solid State **20**, K155 (1967).

[34] A. A. Bolzan, C. Fong, B. J. Kennedy, and C. J. Howard, J. Solid State Chem. **113**, 9 (1994).

[35] G. Beamson, D. Briggs, S. F. Davies, I. W. Fletcher, D. T. Clark, J. Howard, U. Gelius, B. Wannberg, and P. Balzer, Surf. Interface Anal. **9**, 541 (1990).

[36] R. H. Day, P. Lee, E. P. Saloman, and D. J. Nagel, J. Appl. Phys. **52**, 6965 (1981).

[37] F. H. Jones, K. Rawlings, J. S. Foord, R. G. Egdell, J. B. Pethica, B. M. R. Wanklyn, S. C. Parker, and P. M. Oliver, Surf. Sci. **359**, 107 (1996).

[38] K. Yoshimura, T. Miki, S. Iwama, and S. Tanemura, Thin Solid Films **282**, 235 (1996).

[39] B. O. Marinder, Acta Chem. Scand. **15**, 707 (1961).

[40] K. Sakata, J. Phys. Soc. Jpn. **26**, 582 (1969).

[41] J. F. Marucco, R. Tetot, P. Gerdanian, and C. Picard, J. Solid State Chem. **18**, 97 (1976).

[42] C. N. R. Rao, G. R. Rao, and G. V. Subba Rao, J. Solid State Chem. **6**, 340 (1973).

[43] S. M. Shapiro, J. D. Axe, G. Shirane, and P. M. Racah, Solid State Commun. **15**, 377 (1974).

[44] J. B. Goodenough, Prog. Solid State Chem. **5**, 145 (1971).

[45] N. Beatham, P. A. Cox, R. G. Egdell, and A. F. Orchard, Chem. Phys. Lett. **69**, 479 (1980).

[46] A. Kotani and Y. Toyazawa, J. Phys. Soc. Jpn. **37**, 912 (1974).

[47] J. N. Chalzalviel, M. Campagna, G. K. Wertheim, and H. R. Shanks, Phys. Rev. B **16**, 697 (1977).

[48] G. K. Wertheim, Chem. Phys. Lett. **65**, 377 (1979).

[49] Y. J. Kim, Y. Gao, and S. A. Chambers, Appl. Surf. Sci. **120**, 250 (1997).

[50] R. G. Egdell, S. Eriksen, and W. R. Flavell, Solid State Commun. **60**, 835 (1986).

[51] R. Dixon, R. G. Egdell, and G. Beamson, J. Chem. Soc., Faraday Trans. **91**, 3495 (1995).

[52] R. G. Egdell and S. C. Parker, in *Science of Ceramic Interfaces*, edited by J. Nowotny (Elsevier, Amsterdam, 1991).

[53] Z. Zhang, S. P. Jeng, and V. E. Henrich, Phys. Rev. B **43**, 12 004 (1990).

[54] D. Morris, R. Dixon, F. H. Jones, Y. Dou, R. G. Egdell, S. W. Downes, and G. Beamson, Phys. Rev. B **55**, 16 083 (1997).

[55] S. Shin, S. Suga, M. Taniguchi, M. Fujisawa, H. Kanzaki, A. Fujimori, H. Daimon, Y. Ueda, K. Kosuge, and S. Kachi, Phys. Rev. B **41**, 4993 (1990).

[56] A. Howard, C. E. J. Mitchell, D. Morris, R. G. Egdell, and S. C. Parker Surf. Sci. (to be published).

[57] M. Sander and T. Engel, Surf. Sci. **302**, L263 (1994).

[58] D. Novak, E. Garfunkel, and T. Gustafsson, Phys. Rev. B **50**, 5000 (1994).

[59] S. Fischer, A. W. Munz, K. D. Schierbaum, and W. Göpel, Surf. Sci. **337**, 17 (1995).

[60] P. W. Murray, N. G. Condon, and G. Thornton, Phys. Rev. B **51**, 10 989 (1995).

[61] H. Onishi and Y. Iwasawa, Chem. Phys. Lett. **226**, 111 (1994).

[62] U. Diebold, J. Lehman, T. Mahmoud, M. Kuhn, G. Leonardelli, W. Hebenstreit, M. Schmid, and P. Varga, Surf. Sci. **411**, 137 (1998).

[63] P. M. Oliver, G. W. Watson, E. T. Kelsey, and S. C. Parker, J. Mater. Chem. **7**, 563 (1997).

[64] H. Onishi and Y. Isasawa, Chem. Phys. Lett. **226**, 111 (1994).

[65] U. Diebold, W. Hebenstreit, G. Leomardelli, M. Schmid, and P. Varga, Phys. Rev. Lett. **81**, 405 (1998).

[66] U. Diebold, J. F. Anderson, K. O. Ng, and D. Vanderbilt, Phys. Rev. Lett. **77**, 1322 (1996).

[67] M. Valigi, D. Cordischi, G. Minelli, P. Natale, P. Porta, and C. P. Kejizers, J. Solid State Chem. **77**, 255 (1988).

[68] R. S. Roth and L. W. Coughanour, J. Res. Natl. Bur. Stand. **55**, 209 (1955).

[69] A. D. Waldsley, Acta Crystallogr. **14**, 660 (1961).

[70] D. Briggs and M. P. Seah, *Practical Surface Analysis* (Wiley, New York, 1983).

[71] B. Poumellec, F. Lagnel, J. F. Marucco, and B. Touzelin, Phys. Status Solidi B **133**, 371 (1986).

[72] F. Lagnel, B. Poumellec, and R. Cortes, J. Phys. Chem. Solids **50**, 1211 (1989).

[73] M. R. Antonio, I. Song, and H. Yamada, J. Solid State Chem. **93**, 183 (1991).

[74] B. Poumellec, J. F. Marucco, and B. Touzelin, Phys. Status Solidi B **137**, 519 (1986).

[75] S. H. Vosko, L. Wilck, and M. Nusair, Can. J. Phys. **58**, 1200 (1980).

[76] M. Casarin, C. Maccato, and A. Vittadini, Phys. Chem. Chem. Phys. **1**, 3793 (1999).

[77] M. Casarin, E. Tondello, and A. Vittadini, Surf. Sci. **387**, L1079 (1994).

[78] M. Casarin, C. Maccato, and A. Vittadini, Chem. Phys. Lett. **280**, 53 (1997).

[79] M. Casarin, C. Maccato, and A. Vittadini, J. Phys. Chem. B **102**, 10745 (1998).

[80] M. Casarin, C. Maccato, and A. Vittadini, Appl. Surf. Sci. **142**, 196 (1999).

[81] J. J. Yeh and I. Lindau, At. Data Nucl. Data Tables **32**, 1 (1985).